JOURNAL OF THE ROYAL SOCIETY Interface

J. R. Soc. Interface (2011) **8**, 807–816
doi:10.1098/rsif.2010.0533
Published online 3 December 2010

Time-resolved vortex wake of a common swift flying over a range of flight speeds

P. Henningsson*,†, F. T. Muijres and A. Hedenström

Department of Theoretical Ecology, Lund University, 223 62 Lund, Sweden

The wake of a freely flying common swift (*Apus apus* L.) is examined in a wind tunnel at three different flight speeds, 5.7, 7.7 and 9.9 m s^{-1}. The wake of the bird is visualized using high-speed stereo digital particle image velocimetry (DPIV). Wake images are recorded in the transverse plane, perpendicular to the airflow. The wake of a swift has been studied previously using DPIV and recording wake images in the longitudinal plane, parallel to the airflow. The high-speed DPIV system allows for time-resolved wake sampling and the result shows features that were not discovered in the previous study, but there was approximately a 40 per cent vertical force deficit. As the earlier study also revealed, a pair of wingtip vortices are trailing behind the wingtips, but in addition, a pair of tail vortices and a pair of 'wing root vortices' are found that appear to originate from the wing/body junction. The existence of wing root vortices suggests that the two wings are not acting as a single wing, but are to some extent aerodynamically detached from each other. It is proposed that this is due to the body disrupting the lift distribution over the wing by generating less lift than the wings.

Keywords: common swift; *Apus apus*; aerodynamics; wake; particle image velocimetry (DPIV); wind tunnel

1. INTRODUCTION

As a flying animal in active flapping flight propels itself through the air it generates periodic disturbances in the air that are left behind the animal as trailing wake vortices. Newton's Third Law dictates that the forces exerted by the animal on the fluid are equal and opposite to the forces exerted by the fluid on the animal. Thus, the wake represents the combined consequences of all wing, body and tail actions. In wakes where vertical flow is dominant over accelerated potential flow [1] and wake dissipation and interactions are assumed negligible, the quantitative properties of the vortices in the wake and their orientation relative to each other, i.e. the wake topology, are sufficient to describe the forces exerted by the flying animal. Studying the wake of an animal to examine the forces produced is a convenient and rather elegant approach as it involves minimal disturbance to the animal. Digital particle image velocimetry (DPIV) is a technique that has been used to visualize the wake of flying animals (e.g. [2–12]). The technique has been greatly developed in recent years and today stereo systems with high-repetition rates exist. In this paper, the results of high-speed stereo DPIV measurements of flapping flight in the common swift (*Apus apus* L.) using such a system are reported. The flapping flight of the swift at cruising speed has been previously studied in the Lund wind tunnel using a two-dimensional DPIV system with 10 Hz repetition rate [7]. The high-repetition rate of the system used in the current study allows for increased time resolution compared with the previous study, which results in higher detail of the final wake representation, both qualitatively and quantitatively. The topology and variation of the quantitative properties of the vortex wake can be sampled within wingbeats instead of, as in the previous study, having to patch together the complete wake from frames originating from separated wingbeats (for examples, of high-speed DPIV, e.g. [11,13–15]). The main objective of the present study was to explore a wider speed range and to derive a time-resolved wake representation by the use of a high-speed stereo DPIV system. The bird was flown at three speeds, covering the complete range of flight speeds possible for the swift in the wind tunnel.

*Author for correspondence (per.henningsson@zoo.ox.ac.uk).
†Present address: Department of Zoology, University of Oxford, Oxford OX1 3PS, UK.

2. MATERIAL AND METHODS

2.1. Birds

Two juvenile common swifts were captured in their nest in the early morning on their assumed fledging day, 4 August 2008, and immediately transported to the wind tunnel facility at Lund University, Sweden. Between flight episodes, they were kept in a lidless plastic box (0.5 × 0.4 m) with an artificial nest bowl. They were hand fed every other hour from morning to evening with

Received 29 September 2010
Accepted 9 November 2010

a mixture of insects, vitamins and water using a syringe. The masses of the birds were monitored carefully throughout the day. Both birds were flying well, but only one of the birds turned out to be suitable for experiments (behaving calmly and flying steadily and at the appropriate location), and therefore all data presented in this paper were collected from this bird. The morphological details of the bird are presented in table 1. Wing area and wing span were measured using Scion Image (Scion Corporation) from top-view digital photographs of the bird with fully spread wings held over a background with a reference grid. Body mass was measured with an electronic balance and averaged over the time of the complete study. On 14 August, both birds were released into the wild.

2.2. Wind tunnel

The Lund University wind tunnel is a closed-circuit, low-turbulence, low-speed wind tunnel designed for experiments with live animals. Details and specifications of the tunnel are described in Pennycuick *et al.* [16]. The air speed across 97 per cent of the test section is within ± 1.3 per cent of the mean [16] and the baseline turbulence is approximately 0.03 per cent [10].

2.3. Stereo digital particle image velocimetry

2.3.1. Specifications, setup and calibration. Flow field areas of approximately 20×20 cm were captured using two CMOS-sensor cameras (High-SpeedStar3: 1024×1024 pixels) connected to frame grabber peripheral component interconnect boards in a PC host. The cameras were equipped with 60 mm lenses (AF Micro Nikkor 60 mm f/2.8D) set to aperture 2.8. The tunnel was filled with a thin fog (particle size 1 μm) that was illuminated by a pulsed 50 mJ laser (Litron LPY732 series, Nd : YAG, 532 nm) at a repetition rate of 200 Hz (10 ns time accuracy). The laser beam was spread by a cylinder lens into a thin sheet shining from above through the glass roof of the test section and transverse to the flow covering the view of the two cameras (figure 1). The cameras were equipped with band pass filters (530 ± 5 nm) blocking light from any light sources other than the laser. The system was operated using DaVis 7.2.2 software package (LaVision, Göttingen, Deutschland, Germany). A high-speed camera (NAC Hotshot 1280) filmed the bird from above at 250 fps to record flight behaviour and the position of the bird in relation to the laser sheet during each measurement.

The DPIV cameras were calibrated using the calibration routine in DaVis. The routine involved a calibration plate (20×20 cm, type 22) used to calculate the orientation of each of the two cameras. The calibration was also fine tuned with a self-calibration routine, also included in DaVis, which compensates for any misalignments between the laser sheet and the calibration plate.

In order to optimize pixel displacement between image pairs, the time delay between these images (dt) was tested on background flow. The time delay was chosen that resulted in 3–5 pixels displacement.

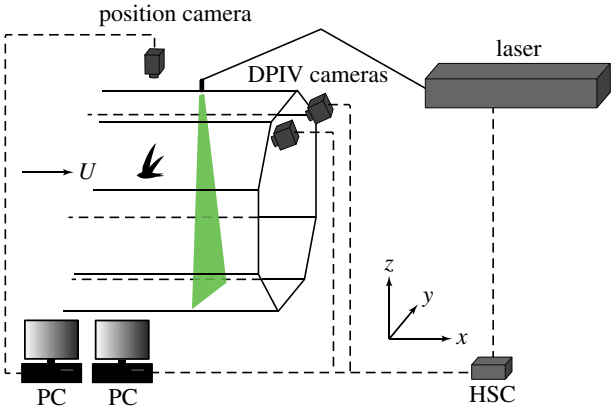

Figure 1. Experimental setup for visualizing the wake of the flying swift. The tunnel is filled with a thin fog that is illuminated by the pulsed laser emitting 200 pulse pairs per second. The laser is synchronized with the two CMOS DPIV cameras that capture images of the smoke at each laser pulse. The images are stored in the host PC. The light emitted from the laser is guided via an optical arm that by the end of it has a lens that spreads the light beam into a thin light sheet. The light sheet was for this experiment positioned perpendicular to U. The position camera is used for recording the flight behaviour of the bird and its location relative to the laser sheet during measurements. The laser and the cameras are triggered and synchronized by the high-speed controller box (HSC).

Table 1. Morphological details of the bird used in the experiments.

total mass (kg)	0.042
wingspan (m)	0.38
wing area (m^2)	0.014
mean wing chord (m)	0.037
aspect ratio	10.3
body frontal area (m^2)	0.0011

2.3.2. Data acquisition. The stereo DPIV cameras, the laser and the position high-speed camera were all triggered by a common trigger signal manually executed by the operator. Triggering was done when the bird was flying steadily in the appropriate location, i.e. in view of the cameras and 0.3–0.4 m (approx. 8–11 chord lengths) upstream of the laser sheet. Each triggering event lasted 1 s, i.e. recording 200 image pairs. If the bird showed any tendency to move too close to the laser sheet during the measurement, the light was blocked for the safety of the bird by activating an electronic internal shutter in the laser control. The bird was flown at wind tunnels speeds $U_\infty = 5.9$, 7.8 and 10.1 m s^{-1}, or expressed as equivalent air speed, $U_{eq} =$ 5.7, 7.7 and 9.9 m s^{-1} ($U_{eq} = U_\infty \sqrt{\rho/\rho_0}$, where ρ is the average air density measured over the experimental period: 1.17 kg m^{-3} and ρ_0 is the standard air density at sea level; 1.225 kg m^{-3}).

2.3.3. Data analysis. Only sequences corresponding to films from the position camera showing steady flight were used for further analysis. The DPIV data were analysed using DaVis software. The raw images were

pre-processed prior to vector computations, and images were filtered by subtracting a sliding minimum over five frames (two before and two after the current frame). This operation filters out any irrelevant structures, such as streaks in the light owing to imperfections in the glass roof, or if the bird was visible in the background of the images. For image correlation, multi-pass stereo cross-correlation was used (64×64 in initial step and 32×32 in final step, 50% overlap). The resulting vector fields were post-processed, first by deleting vectors that showed a peak ratio less than 1.01, when dividing the highest correlation peak with the second highest correlation peak. Secondly, vectors were deleted if the magnitude was two times the neighbourhood root mean square (RMS) and recalculated if the magnitude was three times the neighbourhood RMS. Thirdly, empty spaces were filled in by interpolation and a 3×3 smoothing average was applied. For each sequence, background velocities based on measurements of background flow were subtracted to obtain images showing only velocities induced by the bird.

The velocity vectors in x- (streamwise), y- (spanwise) and z- (vertical) direction (figure 1) were used to calculate the vorticity normal to each plane. Circulation was calculated for distinct structures in the wake, wingtip vortex, tail vortex and a vortex shed from the wing/body junction (see below), using a custom written MATLAB analysis program (The MathWorks, Inc., Natick, MA, USA) and otherwise following the same procedure as described in Spedding *et al.* [3,4].

In order to visualize the wake topology, the images were compiled into a three-dimensional representation of the wake by converting the time delay between the images ($\Delta t = 1/200$ s) into spatial displacement ($\Delta x = \Delta t U_\infty$) assuming a constant convection solely contributed by the freestream velocity (U_∞). The compiled three-dimensional models were used to generate vorticity iso-surface plots of wakes. The iso-surface plots show the normalized constant streamwise vorticity ($\omega_x^* = \pm 2$, where $\omega_x^* = \omega_x / \overline{|\omega_x|}$).

2.4. Model formulation and force derivations

Circulation was calculated on distinct and identifiable wake structures, namely wingtip vortices, wing root vortices and tail vortices. All of these structures were assumed to reflect consequences of the force generated by the flying bird. Instantaneous force generated as a function of time within the wingbeat is according to the Kutta–Joukowski theorem

$$F_{\text{inst}}(t) = \rho 2 b(t) \Gamma(t) U_\infty, \tag{2.1}$$

where ρ is air density and $\Gamma(t)$ is circulation over time of wingtip, root and tail vortices. $b(t)$ represent the semi-span of the three different wake structures over time, so that if, e.g. the force generated by the wingtip vortices is calculated, $b(t)$ represent the semi-span of the wingtip vortices. In the same manner, $b(t)$ represents semi-span for root- and tail-vortices for the calculation of the forces produced by those structures. Wake period was normalized so that $\tau = t/T$, where T is the wingbeat time duration. Beginning and end of the wingbeat was defined as the upper turning point. The total force over the wingbeat is then

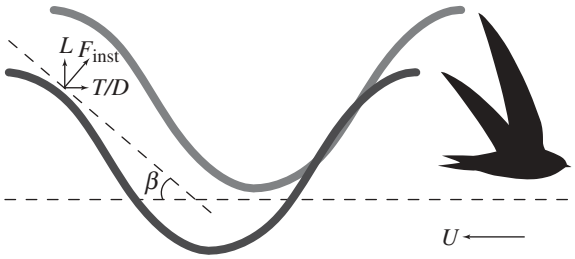

Figure 2. Illustration showing how the angle (β) of the wake plane was measured and used to derive instantaneous vertical force (lift, L) and horizontal force (thrust/drag, T/D) from the total instantaneous force (F_{inst}). The bird is flying form left to right and the two grey trails symbolizes the wingtip vortices left behind in the wake.

$$F_{\text{tot}} = \int_{\tau=0}^{1} F_{\text{inst}}(\tau)\, \mathrm{d}\tau. \tag{2.2}$$

The resulting net force was calculated as the sum of the total force contributed by each of the three vortex structures, wingtip, root and tail vortex. The total force is then

$$F_{\text{tot}}^* = F_{\text{tot,tip}} + F_{\text{tot,root}} + F_{\text{tot,tail}}. \tag{2.3}$$

This force corresponds to the total net force vector generated by the bird, including both lift (vertical force) and thrust (horizontal force). A bird flying level and at constant speed, which was the case with this bird during recording, needs to produce lift and thrust to balance the counter acting weight and drag. For simplicity, thrust/drag force will hereafter be referred to as drag. In order to tease apart lift and drag, the geometry of the wake was taken into account. By tracing the location of the centre of wingtip, root and tail vortices over time (t) and space ($x = tU_\infty$), the three-dimensional path of each of the structures could be estimated. The path was smoothed by the use of a cubic smoothing spline (MATLAB, CSAPS, smoothing parameter set to $1–10^{-3}$). The derivative of this spline was used to estimate the wake plane angle over time (defined as the inclination angle between the wake plane and the horizontal, β; figure 2). The direction of the total force vector previously calculated was assumed to always be normal to the wake plane and subsequently lift (L) was calculated as

$$L = \sum_i \int_{\tau=0}^{1} F_{\text{inst},i}(\tau) \cos(\beta_i(\tau))\, \mathrm{d}\tau \tag{2.4}$$

and drag (D) as

$$D = \sum_i \int_{\tau=0}^{1} F_{\text{inst},i}(\tau) \sin(\beta_i(\tau))\, \mathrm{d}\tau, \tag{2.5}$$

where i denotes wingtip, root and tail forces calculated according to equation (2.1) and $\beta_i(\tau)$ is the wake plane angle over time for wingtip and wing root. For the tail, the angle is assumed to be zero, ($\beta_{\text{tail}} = 0$), so only lift is produced.

3. RESULTS

3.1. Overall wake topology

The fundamental structure of the swift wake consists of pairs of wingtip vortices, wing root vortices and tail vortices. Figure 3 shows a typical sequence for each speed, 5.7, 7.7 and 9.9 m s^{-1}, of selected wake images of the left wing and tail.

The beginning of downstroke is similar for all speeds, the wingtip vortex is starting to form but no root vortex is present (figure 3*a*,*f*,*k*). At 5.7 m s^{-1}, tail vortices are visible during the start of the downstroke (figure 3*a*). At mid-downstroke both the wingtip vortex and the wing root vortex are the strongest at all speeds (figure 3*b*,*g*,*l*). The end of downstroke shows weaker wingtip and root vortices than previously in the wing stroke and a tail vortex is present at 5.7 m s^{-1} (figure 3*c*), which is absent at 7.7 m s^{-1} at this stage of the wingbeat (figure 3*h*). Also at 9.9 m s^{-1}, a tail vortex is present, but counter-rotating to the wingtip vortex (figure 3*m*). Mid-upstroke shows wingtip vortices at all speeds, but no root vortices (figure 3*d*,*i*,*n*). At 5.7 m s^{-1}, the tail vortex has grown stronger than previously in the wingbeat (figure 3*d*) and at 9.9 m s^{-1}, the opposite-signed tail vortex is still present (figure 3*n*). At the end of upstroke, at all speeds, the wingtip vortex has decreased in strength from the peak earlier in the wingbeat to a point where it is hardly distinguishable. The tail vortex is present at 5.7 m s^{-1} (figure 3*e*) and 7.7 m s^{-1}(figure 3*j*), but not at 9.9 m s^{-1}(figure 3*o*).

At the lowest speed (5.7 m s^{-1}), we analysed five separate flight sequences consisting of eight wingbeats; for the medium flight speed (7.7 m s^{-1}) seven separate flights consisting of 20 wingbeats were analysed; for the highest speed (9.9 m s^{-1}), we analysed six separate flight sequences consisting of 12 wingbeats. One wingbeat consisted of on average 22 PIV frames. The vorticity iso-surface plots (iso-value 60 s^{-1}) show the streamwise vorticity trailing the swift during a little over one wingbeat, starting from the beginning of the downstroke (figure 4). At 5.7 m s^{-1}, wingtip vortices are prominent during the downstroke (figure 4*a*). Wing root vortices are formed at an early stage of the downstroke, but decreases to a non-visible, below threshold, strength by the end of the downstroke. During the early upstroke, the tail vortices are increased to a considerable strength and are by the end of the upstroke the only visible structure above the threshold. During the course of the final half of the upstroke, wingtip vortices merge with the tail vortices (figure 5; mean tail wake-span is 27 mm during mid-upstroke). At 7.7 m s^{-1}, the downstroke shows similar features as that of 5.7 m s^{-1} (figure 4*b*), although the wing root vortices appear to be present for a larger portion of the downstroke, especially at the end of downstroke, as compared with 5.7 m s^{-1}. The upstroke at 7.7 m s^{-1}, similar to 5.7 m s^{-1}, also shows how the root vortices fall below the threshold value and the wingtip vortices merge with the tail vortices (mean tail wake-span is 28 mm at mid-upstroke), but at this speed the tail vortices are weaker compared with those at 5.7 m s^{-1}. At 9.9 m s^{-1}, the circulation is overall lower than at 5.7 and 7.7 m s^{-1}. During the beginning of the downstroke, wing root vortices are formed and stay present throughout the downstroke, similarly to 7.7 m s^{-1} (figure 4*c*). The wingtip vortices that can be seen in the vorticity vector field images during the mid-upstoke (figure 3*n*) are too weak to appear in the iso-surface plots and hence the upstroke shows no wake structures.

3.2. Quantitative wake measurements

At all speeds, the dominant wake structures were the wingtip vortices, the wing root vortices and the tail vortices. Measured circulation of these vortex structures are presented in figure 6, where the fitted lines show the cubic spline functions used in the model. At all three speeds, there is a rapid increase of wingtip circulation during the first half of the downstroke, reaching a peak at mid-downstroke (figure 6*a*,*d*,*g*). At $U=$ 5.7 m s^{-1}, there is a steeper increase of Γ compared with 7.7 and 9.9 m s^{-1} (figure 6*a*). The wing root circulation follows the pattern of the wingtip circulation, although with opposite sign, i.e. a rapid increase in $|\Gamma|$ during the first half of the downstroke and with peak at the same time as the wingtip circulation, suggesting that the two structures are correlated (figure 6*b*,*e*,*h*). The overall magnitude of wingtip circulation and wing root circulation shows a decrease with increasing speed. Tail circulation, for all speeds, follows an opposite pattern to the wingtip circulation, i.e. when wingtip circulation is low, as in beginning and end of the wing stroke, the tail circulation is high and vice versa. Tail circulation is on average higher at 5.7 m s^{-1} than at 7.7 and 9.9 m s^{-1} (figure 6*c*,*f*,*i*).

3.3. Force derivations

The model used to estimate forces generated by the bird included the three major structures of the wake, i.e. wingtip, wing root and tail vortices. The total aerodynamic force was calculated according to equations (2.1)–(2.3) and evaluated to 0.39 N for 5.7 m s^{-1}, 0.34 N for 7.7 m s^{-1} and 0.48 N for 9.9 m s^{-1}. The total force vector represents both lift and thrust combined of the bird and therefore an attempt was made to separate these components according to equations (2.4) and (2.5). Lift was then calculated as 0.23 N (56% of weight) for 5.7 m s^{-1}, 0.24 N (58% of weight) for 7.7 m s^{-1} and 0.23 N (56% of weight) for 9.9 m s^{-1}. The weight of the bird was 0.41 N, calculated based on its average mass during the experimental period (table 1). Drag was estimated at 0.043 N for 5.7 m s^{-1}, 0.041 N for 7.7 m s^{-1} and 0.030 N for 9.9 m s^{-1}. Consequently, the lift-to-drag ratio (L/D) for the swift according to this model was 5.3 for 5.7 m s^{-1}, 5.9 for 7.7 m s^{-1} and 7.7 for 9.9 m s^{-1}, respectively. To test the model's sensitivity to the estimate of wake plane angle, the smoothing parameter was altered and the change in lift and drag was examined. Decreasing the smoothing parameter to $1–10^{-2}$ resulted in an unchanged estimate of lift and a reduction in drag to 0.035 N. Increasing the smoothing

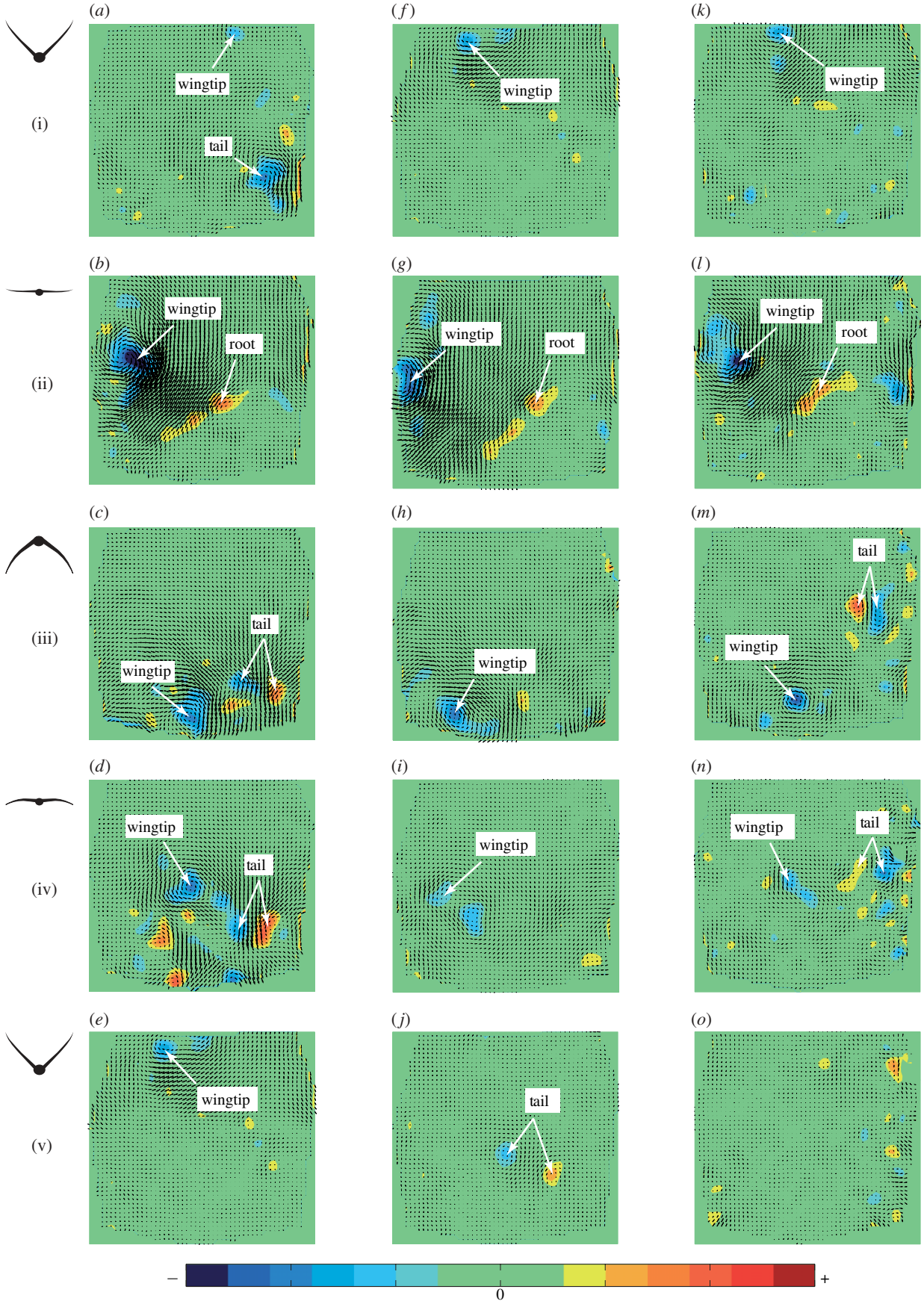

Figure 3. Velocity vector field superimposed on colour-coded vorticity field of key phases of the wingbeat for each speed. (*a*,*f*,*k*) 5.7 m s^{-1}, (*b*,*g*,*l*) 7.7 m s^{-1} and (*c*,*h*,*m*) 9.9 m s^{-1}. (i) shows beginning of downstroke, (ii) shows mid-downstroke, (iii) shows end of downstroke, (iv) shows mid-upstroke and (v) shows end of upstroke. Bird silhouettes symbolize the different phases of the wingbeat. Distance from the swift to the image plane was between 0.3 and 0.4 m, which corresponds to 8–11 chord lengths. The colour map scales from −350 (blue) to +350 s^{-1} (red).

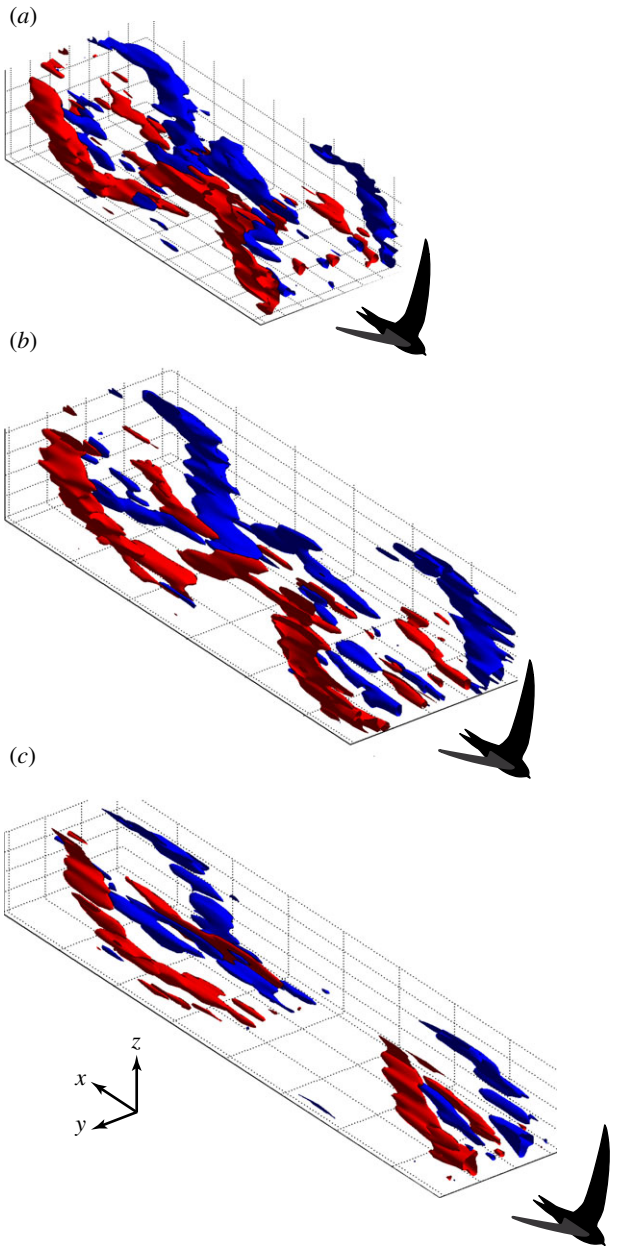

Figure 4. Iso-surfaces showing 1.5 wingbeats for each speed. 31, 33 and 34 images were used to build the three-dimensional plot for 5.7, 7.7 and 9.9 m s^{-1}, respectively. (*a*) 5.7 m s^{-1}. (*b*) 7.7 m s^{-1}. (*c*) 9.9 m s^{-1}. Iso-value is 60 s^{-1}. The view is oriented so as if the bird was flying obliquely towards the observer from left to right. Red-coloured patches represent positive circulation (clockwise rotation as seen in direction of flight) and blue-coloured patches represent negative circulation (counterclockwise rotation as seen in direction of flight).

parameter to $1{-}10^{-6}$ resulted in unchanged lift and drag of 0.035 N.

Lift and drag coefficients for the entire wing/body assembly can be calculated as

$$C_{\mathrm{L}} = \frac{L}{qS} \tag{3.1a}$$

and

$$C_{\mathrm{D}} = \frac{D}{qS}, \tag{3.1b}$$

where $q = \rho U_{\infty}^2/2$ is the dynamic pressure ($\rho = 1.17$ kg m^{-3}, averaged over the complete experimental period) and S is the wing planform area (table 1). For 5.7 m s^{-1} C_{L} was 1.31 and C_{D} was 0.28, for 7.7 m s^{-1} C_{L} was 0.68 and C_{D} was 0.12 and for 9.9 m s^{-1} C_{L} was 0.56 and C_{D} was 0.07.

4. DISCUSSION

4.1. Flight characteristics

The flight characteristics of the swift used in this experiment was largely similar to that described for the experimental bird by Henningsson *et al.* [7]. The bird flew well after just 1 day of training. Unlike the bird used by Henningsson *et al.* [7], the current bird would fly at a slightly wider range of flight speeds, from 5.7 to 9.9 m s^{-1}, which allowed for an extension of the examined range. At 5.7 m s^{-1}, the bird was clearly struggling to stay aloft, with spread tail and high body angle. Below this speed, it would descend to the floor of the test section within a few seconds. At 9.9 m s^{-1}, the bird was flying in a more relaxed way than at 5.7 m s^{-1}, but at this speed, manoeuvring in relation to the wind tunnel walls started to become challenging for the bird and consequently it was not possible to examine higher flight speeds owing to safety issues.

It is important to acknowledge that the results in this study are based on only one single individual and that this obviously is a limitation to the study.

4.2. Wake topology

The wake topology of the swift as interpreted from the wake images captured at the transverse plane and the corresponding three-dimensional vorticity iso-surface plots show a more complex wake than previously described. In Henningsson *et al.* [7], longitudinal (sagittal) wake data led to the conclusion that the wake consisted mainly of a pair of trailing wingtip vortices and between these were interconnecting vortex filaments. The present data suggest that the wake structure consists of some additional features. The wingtip vortices show very similar features as that described in Henningsson *et al.* [7]. In addition, distinct and clear wing root vortices are found, that appear to originate from a point near the wing/body junction. The root vortices are very consistent and present in every wingbeat at all examined speeds. The existence of root vortices indicates that the wing/body configuration is not acting as a single wing but rather the wings operate to some extent aerodynamically detached from each other. However, since the circulation in the root vortex is lower than that of the wingtip vortex there must be some circulation also over the body/tail and therefore the wakes of the wings are not completely isolated. This is similar to what has been found in the wake of bats [6,9,11,15], a blackcap (*Sylvia atricapilla*; [14]) and to some extent in bumble-bees [17]. During the downstroke, the strength of the root vortex relative to the tip vortex was higher in the swift compared with the blackcap, while it is difficult to compare the wakes

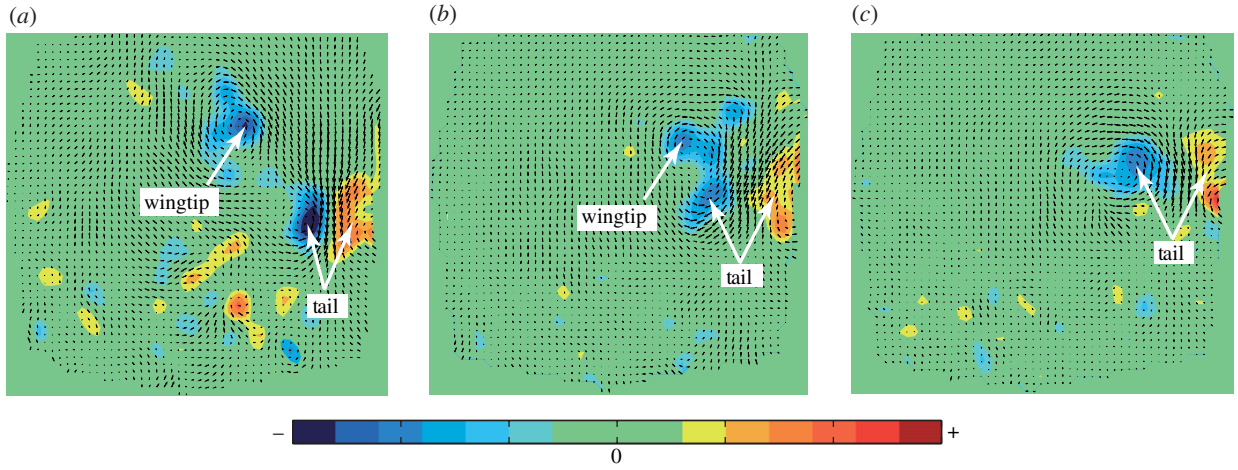

Figure 5. Illustration showing how the wingtip vortex merges with the tail vortex during the upstroke at the slowest speed, 5.7 m s^{-1}. The left image (*a*) shows the two structures when they still are distinctly separated. The centre image (*b*) was captured three frames later than the left ($\mathrm{d}t = 3/200$ s) and shows how the wingtip vortex has moved towards the tail vortex and has started to merge with it. The right image (*c*) was, in turn, captured three frames later than the left ($\mathrm{d}t = 3/200$ s) and shows when the two vortex structures have merged completely.

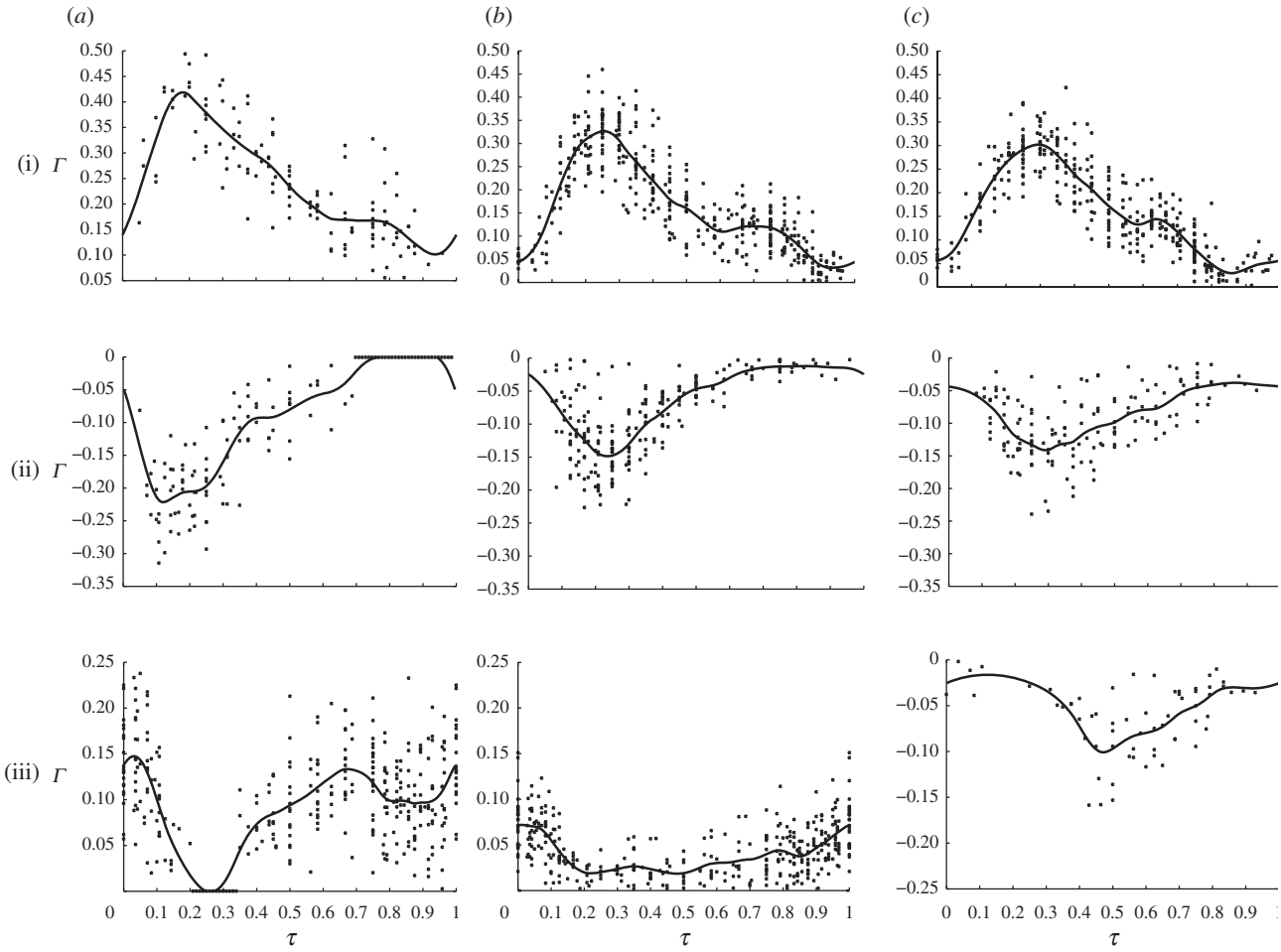

Figure 6. Circulation over the wingbeat in wingtip vortex, wing root vortex and tail vortex. The cubic smoothing splines used when calculating forces from the model are plotted in each panel. Circulation in sections within wingbeat that contain no data because the structure in question was not visible has been set to zero. (*a*) shows the results for 5.7 m s^{-1}, (*b*) shows results for 7.7 m s^{-1} and (*c*) shows results for 9.9 m s^{-1}. (i) shows wingtip circulation, (ii) shows wing root circulation and (iii) shows tail circulation. In all plots, *x*-axis corresponds to phase in wingbeat (0 is beginning of downstroke, 0.25 mid-downstroke, 0.5 end of downstroke, 0.75 mid-upstroke and 1 end of upstroke) and *y*-axis circulation (Γ).

during the upstroke owing to potential interaction between tip, root and tail vortices in the blackcap arising from its passerine wingbeat kinematics (cf. [14]). The fact that this wake structure is found in such a vast range of organisms, both in terms of morphology, taxonomy and size, suggests that the root vortices originate from the constraint of the necessity to incorporating a solid body into a smooth wing design [17]. The ability to fly has, to our knowledge, evolved independently at least four times during the history of evolution: in insects, birds, bats and the extinct pterosaurs. It may be quite counterintuitive to think that the aerodynamics of animal flight should have evolved to such similar solutions. On the other hand, the body of a bird, bat or insect is likely to always generate less downwash (lift) compared with the wings (e.g. [18,19]), simply because of the aerodynamic properties of such shapes and therefore there will be a steep pressure gradient from wing to body. This gradient will necessarily introduce some disturbance to the wake, which could be manifested as root vortices. However, there are examples of animals that have succeeded in this without introducing root vortices, e.g. dragonflies [20]. An alternative explanation to the formation of root vortices may be that because the wing is flapping, a gradient of velocities along the wing is created that could result in a decrease in circulation from the wing tip to the wing base. This gradient may be manifested in the shedding of vortex filaments that subsequently roll-up to form a root vortex structure. Either way, it is not obvious whether the wake topology with separate loops is an advantage or a constraint. Generating two separate vortex loops, one for each wing, will be less efficient than if the two wings together with the body would act as one wing and only shed wingtip vortices. On the other hand, separate wakes may facilitate increased agility, gained from each wing operating aerodynamically detached from the other (see [6]).

A previous study of swift wakes consisted of only longitudinal views [7] and therefore the tail vortices were not well represented and therefore largely ignored. With the current transverse data, the tail vortices are more obvious and consistent and could be incorporated in the wake model. The tail appears to possibly have different functions at the three different speeds. At $5.7\ \mathrm{m\,s^{-1}}$, the tail is widely spread with the circulation of the tail vortices being stronger compared with 7.7 and $9.9\ \mathrm{m\,s^{-1}}$ (figure 6*c*). However, the reason that the circulation of the tail vortices at the lowest speed is higher than at the other speeds may not only be due to a wider spread of the tail, but also to a higher body angle. The body angle of a flying bird has been shown earlier to affect the tail vortices [19]. The body angle of the swift was, however, not measured in this study. At $7.7\ \mathrm{m\,s^{-1}}$, the circulation is lower than at $5.7\ \mathrm{m\,s^{-1}}$ (figure 6*f*) and at $9.9\ \mathrm{m\,s^{-1}}$, the circulation is of opposite sign compared with 5.7 and $7.7\ \mathrm{m\,s^{-1}}$ (figure 6*i*). Especially at $5.7\ \mathrm{m\,s^{-1}}$, but also at $7.7\ \mathrm{m\,s^{-1}}$, the circulation of the tail vortices follows inversely that of the wingtip vortices. This implies that the tail has the function of contributing lift during periods of the wing stroke when the lift generated by the wings is low. At $9.9\ \mathrm{m\,s^{-1}}$, the tail shows reversely rotating vortices compared with those at 5.7 and $7.7\ \mathrm{m\,s^{-1}}$, actually generating negative lift. At that speed it is possible that the tail is used for control, for example, by creating a pitch up moment to counteract a pitch down moment introduced by the wings. This configuration would result in longitudinal static stability (e.g. [21]). However, it is important to acknowledge that, since the bird is flying in a confined volume and not in the open airspace as it would in natural flight, this sort of adjustment may be due to the bird trying to fly steadily in the wind tunnel. On the other hand, the pattern is consistent over wingbeats, which would not be expected if it was due only to stabilizing manoeuvres.

4.3. Model and force derivations

The model describing the wake of the swift accounts for the three major structural components of the wake, i.e. wingtip, root and tail vortices. Weight of the bird is the force best known in this type of experiments and it is used as a reference for the model output. The results show that the lift calculated from the wake-based model is only about 50–60% of the weight of the bird. This deficit is a concern, since it indicates that the wake representation is not fully satisfactory. The method of measuring the circulation, the model formulation and finally the calculations performed have been carefully checked and there is no reason to suspect any methodological errors or calculation errors. A similar problem was addressed by Hubel *et al.* [13], where wake circulation yields approximately 50 per cent weight support for a bat in flapping flight. In that study, two potential explanations were proposed: firstly, that vortex structures are partly destroyed by background turbulence or other unsteady phenomena, and secondly, that a portion of the vortex sheet is lost owing to diffusion before it converges into the wingtip vortex. Both of these explanations are potentially applicable to the current case of the swift. Both Hubel *et al.* [13] and the current study of the swift measured the far wake behind the animals. It is possible that the wake evolves when convecting downstream of the animal into a structure more or less distorted compared with the original wake created at the wing. The amount of distortion thus depends on how far downstream the wake is sampled. Yet another potential explanation to the wake deficit is that the wingtip vortex and the wing root vortex interact. In aeronautics, there is a well-known phenomenon commonly called Crow instability [22], in which vortex pairs interact as the wake evolves in an increasingly complex way further downstream of a wing. This phenomenon has been empirically investigated at $Re_\Gamma \approx 10^5$ ($Re_\Gamma = (\Gamma_1 + \Gamma_2)/\nu$, where Γ_1 and Γ_2 are the circulation in the two vortices and ν is the kinematic viscosity; corresponding value for the swift was approx. 2.4×10^4) and the results suggest that counter-rotating vortex pairs interact by initially attracting towards each other and subsequently the weaker (in this case root) vortex inter-twists the stronger (in this case wingtip) vortex and finally wraps around it into a complex structure

[23]. The wake of the swift was sampled approximately 8–10 chord lengths downstream from the bird, which suggests that the wake, when captured, is in its early state of Crow instability. However, it is possible that the two pairs of vortices, wingtip and root, have interacted so that the wing root vortex has started to move towards the wingtip vortex and vice versa. If this is the case, the effective wake span will be affected in two ways: the wingtip vortex will move inwards from the wingtip and the root vortex will move outwards from the wing root, resulting in an underestimate of the wingtip vortex span and an overestimate of the root vortex span. These effects will both reduce the positive contribution to lift by the wingtip vortex and increase the negative contribution to lift generated by the root vortex (equation 2.1). Even at an early state of Crow instability this could potentially cause a misrepresentation of the wake and an underestimate of the forces. To test this, the model was adjusted so that the measured wake span was equal to the span of the bird, i.e. as if no contraction in the wake occurred. Then, the calculated lift was 95, 83 and 115 per cent of the weight for 5.7, 7.7 and 9.9 $\mathrm{m\,s^{-1}}$, respectively. The L/D ratio was, however, almost the same, 5.2, 5.8 and 8.0, for the three speeds, respectively. This result is probably an overestimate of the forces, since it is expected that the wake contracts downstream the bird (e.g. [24]), but it represents the other extreme, i.e. no wake contraction, and the results from these two calculations (based on actual wake span versus based on wing span) should encircle the true value. If the deficit indeed stems from Crow instability, the circulation in the wake would be conserved (cf. [25]) and not lost or destroyed as proposed by Hubel *et al.* [13]. To examine this, the circulation measured in the wake in the present study was compared with the circulation measured in Henningsson *et al.* [7], where the wake was measured in a longitudinal plane. The circulation measured in the current study was not different from that found in the earlier study of the wake of a flying swift. This supports the argument that the wake deficit found in the current study is due to some wake distortion, for example, Crow instability. If this is true, it is a general issue when studying far wakes at the transverse plane. It is a dilemma, if the wake is sampled close to, but not on the object, the samples will represent a wake that is still in an intermediate phase of contraction of unknown degree, whereas if the wake is sampled further downstream where the wake has contracted fully, instability becomes an issue. Furthermore, it is difficult to measure wakes using DPIV on, or very close to, a live animal flying freely in a wind tunnel, owing to safety issues, which means that one is often restricted to measuring the far wake. A detailed study of the development of wingtip and root vortices from close to the wing to far down the wake needs to be done to examine this potential phenomenon.

When a bird is flying level at a fixed velocity, the mean thrust and drag are balanced. Thrust, and hence drag, was estimated by taking the geometry of the wake into account. This calculation rests on the assumptions that the total force (vector sum of lift and thrust) always is generated normal to the wake plane and that the wake plane does not change orientation to a large extent from when it was generated at the wing until it is captured by the DPIV cameras approximately 8–10 wing chords downstream. By comparing near and far wakes of a bat, Johansson *et al.* [8] showed that the qualitative and quantitative wake properties show rather small changes with distance from the object. Nevertheless, the drag estimate made here should be viewed upon as a preliminary estimate, especially considering the above mentioned problem with wake distortion. An alternative model by Henningsson *et al.* [7] used input from longitudinal DPIV images and it was assumed that any shed circulation in the wake corresponded to a change in circulation of the bound vortex on the wing. Otherwise, the calculations were made in a similar fashion as with the current model, by integrating over the wingbeat to calculate the total net force and decomposing this force into lift and thrust based on the geometry of the wake. The L/D ratio estimated by Henningsson *et al.* [7] was 6.7 (an error in the calculation resulted in an erroneous L/D in the original paper) at 8.4 $\mathrm{m\,s^{-1}}$. The closest comparable speed in the current study was 7.7 $\mathrm{m\,s^{-1}}$, and at that speed the measured L/D was 5.9. The L/D ratios for robins were estimated from the wake and evaluated at 7.5 in flapping flight in a wind tunnel [26], which suggests that the L/D ratio measured here is an underestimated value considering the morphological differences between the swift and robin ($AR_{\mathrm{swift}} = 10.3$, $AR_{\mathrm{robin}} = 4.8$). The L/D ratio of the swift in gliding flight in a wind tunnel has been estimated at 12.7 [27]. This represents the true L/D ratio while the L/D ratio calculated here for flapping flight represents the effective L/D (i.e. when the wake geometry owing to the flapping motion is taken into account), which is expected to be lower. However, the fact that the L/D in flapping flight is found to be almost half of that in gliding in the same species is perhaps surprising and more research on this in other flying animals may be worthwhile in order to investigate if the pattern is recurring or if it is something that is characteristic of common swifts.

Capture of swifts and use in experiments was approved by the Ethics Committee at Lund University.

We are thankful to Jan Holmgren for providing the two juvenile swifts and Teresa Kullberg for invaluable help during the experiments. This study was financially supported by grants from the Swedish Research Council and the Knut and Alice Wallenberg Foundation. A.H. is a Royal Swedish Academy of Science Research Fellow supported by grants from the Knut and Alice Wallenberg Foundation.

REFERENCES

1 Dabiri, J. O. 2005 On the estimation of swimming and flying forces from wake measurements. *J. Exp. Biol.* **208**, 3519–3532. (doi:10.1242/jeb.01813)

2 Bomphrey, R. J., Lawson, N. J., Harding, N. J., Taylor, G. K. & Thomas, A. L. R. 2005 The aerodynamics of *Manduca sexta*: digital particle image velocimetry analysis of the leading-edge vortex. *J. Exp. Biol.* **208**, 1079–1094. (doi:10.1242/jeb.01471)

3 Spedding, G. R., Hedenström, A. & Rosén, M. 2003 Quantitative studies of the wakes of freely flying birds in a low-turbulence wind tunnel. *Exp. Fluids* **34**, 291–303. (doi:10.1007/s00348-002-0559-8)

4 Spedding, G. R., Rosén, M. & Hedenström, A. 2003 A family of vortex wakes generated by a thrush nightingale in free flight in a wind tunnel over its entire natural range of flight speeds. *J. Exp. Biol.* **206**, 2313–2344. (doi:10.1242/jeb.00423)

5 Bomphrey, R. J. 2006 Insects in flight: direct visualization and flow measurements. *Bioinspir. Biomim.* **1**, S1–S9. (doi:10.1088/1748-3182/1/4/S01)

6 Hedenström, A., Johansson, L. C., Wolf, M., von Busse, R., Winter, Y. & Spedding, G. R. 2007 Bat flight generates complex aerodynamic tracks. *Science* **316**, 894–897. (doi:10.1126/science.1142281)

7 Henningsson, P., Spedding, G. R. & Hedenström, A. 2008 Vortex wake and flight kinematics of a swift in cruising flight in a wind tunnel. *J. Exp. Biol.* **211**, 717–730. (doi:10.1242/jeb.012146)

8 Johansson, L. C., Wolf, M., von Busse, R., Winter, Y., Spedding, G. R. & Hedenström, A. 2008 The near and far wake of Pallas' long tongued bat (*Glossophaga soricina*). *J. Exp. Biol.* **211**, 2909–2918. (doi:10.1242/jeb.018192)

9 Muijres, F. T., Johansson, L. C., Barfield, R., Wolf, M., Spedding, G. R. & Hedenström, A. 2008 Leading-edge vortex improves lift in slow-flying bats. *Science* **319**, 1250–1253. (doi:10.1126/science.1153019)

10 Spedding, G. R., Hedenström, A. & Johansson, L. C. 2009 A note on wind-tunnel turbulence measurements with DPIV. *Exp. Fluids* **46**, 527–537. (doi:10.1007/s00348-008-0578-1)

11 Hubel, T. Y., Riskin, D. K., Swartz, S. M. & Breuer, K. S. 2010 Wake structure and wing kinematics: the flight of the lesser dog-faced fruit bat, *Cynopterus brachyotis*. *J. Exp. Biol.* **213**, 3427–3440. (doi:10.1242/jeb.043257)

12 Warwick, D. R., Tobalske, B. W. & Powers, D. R. 2005 Aerodynamics of the hovering hummingbird. *Nature* **435**, 1094–1097. (doi:10.1038/nature03647)

13 Hubel, T. Y., Hristov, N. I., Swartz, S. M. & Breuer, K. S. 2009 Time-resolved wake structure and kinematics of bat flight. *Exp. Fluids* **46**, 933–943. (doi:10.1007/s00348-009-0624-7)

14 Johansson, L. C. & Hedenström, A. 2009 The vortex wake of blackcaps (*Sylvia atricapilla* L.) measured using high-speed digital particle image velocimetry (DPIV). *J. Exp. Biol.* **212**, 3365–3376. (doi:10.1242/jeb.034454)

15 Hedenström, A., Muijres, F. T., von Busse, R., Johansson, L. C., Winter, Y. & Spedding, G. R. 2009 High-speed stereo DPIV measurements of wakes of two bat species flying freely in a wind tunnel. *Exp. Fluids* **46**, 923–932. (doi:10.1007/s00348-009-0634-5)

16 Pennycuick, C. J., Alerstam, T. & Hedenström, A. 1997 A new low-turbulence wind tunnel for bird flight experiments at Lund University, Sweden. *J. Exp. Biol.* **200**, 1441–1449.

17 Bomphrey, R. J., Taylor, G. K. & Thomas, A. L. R. 2009 Smoke visualization of free-flying bumblebees indicates independent leading-edge vortices on each wing pair. *Exp. Fluids* **46**, 811–821. (doi:10.1007/s00348-009-0631-8)

18 Tobalske, B. W., Peacock, W. L. & Dial, K. P. 1999 Kinematics of flap-bounding flight in the zebra finch over a wide range of flight speeds. *J. Exp. Biol.* **202**, 1725–1739.

19 Tobalske, B. W., Jason, W. D., Hearn, W. D. & Warrick, D. R. 2009 Aerodynamics of intermittent bounds of flying birds. *Exp. Fluids* **46**, 963–973. (doi:10.1007/s00348-009-0614-9)

20 Thomas, A. L. R., Taylor, G. K., Srygley, R. B., Nudds, R. & Bomphrey, R. J. 2004 Dragonfly flight: free-flight and tethered flow visualizations reveal a diverse array of unsteady lift-generating mechanisms, controlled primarily via angle of attack. *J. Exp. Biol.* **207**, 4299–4323. (doi:10.1242/jeb.01262)

21 Anderson, J. D. 1989 *Introduction to flight*. New York, NY: McGraw-Hill, Inc.

22 Crow, S. C. 1970 Stability theory for a pair of trailing vortices. *AIAA J.* **8**, 2172–2179. (doi:10.2514/3.6083)

23 Bristol, R. L., Ortega, J. M., Marcus, P. S. & Savas, Ö. 2004 On cooperative instabilities of parallel vortex pairs. *J. Fluid Mech.* **517**, 331–358. (doi:10.1017/S0022112004001016)

24 Milne-Thompson, L. M. 1966 *Theoretical aerodynamics*. New York, NY: Dover.

25 Spedding, G. R., Hedenström, A. H., McArthur, J. & Rosén, M. 2008 The implications of low-speed fixed-wing aerofoil measurements on the analysis and performance of flapping bird wings. *J. Exp. Biol.* **211**, 215–223. (doi:10.1242/jeb.007823)

26 Hedenström, A., Rosén, M. & Spedding, G. R. 2005 Vortex wakes generated by robins *Erithacus rubecula* during free flight in a wind tunnel. *J. R. Soc. Interface* **3**, 263–276. (doi:10.1098/rsif.2005.0091)

27 Henningsson, P. & Hedenström, A. In press. Aerodynamics of gliding flight in common swifts. *J. Exp. Biol.*